A One-Dimensional Arterial Network Model for Bypass Graft Assessment

Arthur R. Ghigo, Salam Abou Taam, Xiaofei Wang, Pierre-Yves Lagrée, Jose-Maria Fullana

Medical Engineering & Physics 00 (2017) 1–19

Medical
Engineering &
Physics

A One-Dimensional Arterial Network Model for Bypass Graft Assessment

A. R. Ghigo[a], S. Abou Taam[a,b], X. Wang[a], P-Y Lagrée[a], J-M Fullana[a]
[a] Sorbonne Universités, UPMC Univ Paris 06
CNRS, UMR 7190, Institut Jean Le Rond d'Alembert, F-75005 Paris
[b] Hôpital Privé Claude Galien, 20 route de Boussy
91480 Quincy-Sous-Sénart

Abstract

We propose an arterial network model based on one-dimensional hemodynamic equations to study the behavior of different vascular surgical bypass grafts in the case of an arterial occlusive pathology: a stenosis of the Right Iliac artery. We investigate the performances of three different bypass grafts (Aorto-Femoral, Axillo-Femoral and cross-over Femoral) depending on the degree of obstruction of the stenosis. Numerical simulations show that all bypass grafts are efficient since we retrieve in each case the healthy hemodynamics downstream of the stenosed region while ensuring at the same time a global healthy circulation. We analyze in detail the behavior of the Axillo-Femoral bypass graft by performing hundreds of simulations where we vary the values of its Young's modulus $[0.1-50\ MPa]$ and radius $[0.01-5\ cm]$. Our analysis shows that the Young's modulus and radius of commercial bypass grafts are optimal in terms of hemodynamic considerations. Our numerical findings prove that this model approach can be used to optimize or plan patient-specific surgeries, to numerically assess the viability of bypass grafts and to perform parametric analysis and error propagation evaluations by running extensive simulations.

Keywords: arterial network, 1D model, stenosis, bypass graft

Word Count : 5701

Corresponding Author

Jose-Maria Fullana

Institut Jean le Rond d'Alembert, UMR CNRS 7190, Tour 55-65 5^{e} étage - Bureau 524

Université Pierre et Marie Curie, 4 Place Jussieu, 75005, Paris

Tel (33) (0) 1 44 27 71 41, Fax (33) (0) 1 44 27 52 59

1. Introduction

Arterial diseases such as stenoses are frequent clinical pathologies, and their prevalence is evaluated from 3% to 10% in the global population with a significant growth from 15% to 20% in persons over 70 years old [1]. Stenoses correspond to the partial or total obstruction of an artery and can cause symptoms going from intermittent claudication to severe ischemia. These symptoms result from a decrease in blood supply as the diseased vessel providing vascularization is narrowed or occluded. When untreated, stenoses can have severe consequences and can lead to the amputation of the stenosed member, especially when they occur in the arteries of the lower members, such as in the Iliac arteries.

When the symptoms are too severe or when medical treatment fails, surgery is necessary to restore blood flow downstream of the stenosed member. This can be done by angioplasty stenting, where the obstructed segment is replaced by a prosthesis (stent) during an endovascular substitution surgery. An alternative solution consists in inserting a bypass graft to redirect the flow of blood from a healthy artery to bypass the obstructed vessel and restore blood flow downstream of the stenosis. In both cases, the mechanical role of these grafts or conduits is to replace or bypass vessels that have become occluded or severely obstructed by a disease process [2].

Numerical studies of local endovascular graft replacements have been reported previously (e.g., [3, 4]). We propose to study instead extracorporeal bypass graft procedures. To do so, we consider a detailed model of the systemic network which presents a stenosis of the Right Iliac artery. In this pathological case, the most common bypass graft configurations are: Aorto-Femoral, Axillo-Femoral and cross-over Femoral, defined by the combination of the name of the healthy or donor artery (Aorto for Aorta, Axillo for Axillary and cross-over for the opposite artery, the Left Femoral Artery) and the name of the receptor artery, in our case the Right Femoral artery which follows distally the narrowed site.

The aim of this communication is to use a one-dimensional (1D) model to compute blood flow in each segment of the considered model network before and after extracorporeal bypass graft surgery. To help clinicians optimize surgical repair, we evaluate the viability of each bypass graft by computing the flow rate and pressure downstream of the stenosed member, which is an a posteriori evaluation of the quality of the surgery. Clinicians often prefer the Aorto-Femoral bypass graft. However, for weak patients who can not tolerate the aortic clamping required to insert the Aorto-Femoral bypass graft, the preferred solution is an extra-anatomic Axillo-Femoral bypass graft [5]. Furthermore, it has the shortest graft survival time among the three previously named bypass grafts ([6, 7]). We therefore study in detail the optimization of the geometrical and mechanical characteristics of the Axillo-Femoral bypass graft. We hope that this numerical approach will be used in the future to define the optimal parameters of new prosthesis and help clinicians plan surgeries.

In the following, we present the numerical model and the model arterial network, as applied to the study of flow through three different arterial bypass graft configurations, along with the results of a parametric study of the Axillo-Femoral bypass graft. We propose only hemodynamic predictions based on fluid mechanics equations, regardless of biological phenomena and their consequences. Nevertheless, we are aware that short term graft failures can be caused by infections or hemorrhages, while long-term failures are the result of intimal hyperplasia of the graft site, with a proliferation and a migration of vascular smooth muscle cells near the arterial wall [6].

2. Numerical Model

To compute the hemodynamics in an artery, we use a set of one-dimensional (1D) equations expressed in terms of the flow rate Q, the cross-sectional area A and the internal average pressure P in the artery. This 1D system of equations results from the integration of the Navier-Stokes equations for an incompressible Newtonian fluid over the cross-sectional area of the artery, leading to the following mass and momentum 1D conservation equations

$$\frac{\partial A}{\partial t} + \frac{\partial Q}{\partial x} = 0, \tag{1}$$

$$\frac{\partial Q}{\partial t} + \frac{\partial}{\partial x}(\frac{Q^2}{A}) + \frac{A}{\rho}\frac{\partial P}{\partial x} = 2\pi\nu\left[r\frac{\partial u_x}{\partial r}\right]_{r=R}, \tag{2}$$

where u_x is the axial velocity, ρ is the fluid density and ν is the kinematic viscosity of the fluid. We set $\rho = 1\ g/cm^3$ and $\nu = 3.5\ 10^{-2}\ cm^2/s$, which are typical values for blood. The internal pressure P is related to the cross-sectional area A through the following relationship

$$P = P_{ext} + \beta(\sqrt{A} - \sqrt{A_0}) + \nu_s\frac{\partial A}{\partial t}, \tag{3}$$

under the assumption that the arterial wall is thin, isotropic, homogeneous, incompressible and that it deforms axisymmetrically with each circular cross-section independently of the others. The parameter β describes the elastic behavior of the wall

$$\beta = \frac{\sqrt{\pi}Eh}{(1-\eta^2)A_0},$$

and the parameter ν_s its viscoelastic behavior, that we describe using a Kelvin-Voigt model [8]

$$\nu_s = \frac{\sqrt{\pi}\rho\phi h}{2\rho(1-\eta^2)\sqrt{A_0}A}.$$

The Young's modulus E, the Poisson ratio η, the viscoelastic coefficient ϕ and the arterial thickness h are given in Table A.1 in Appendix A. More details can be found elsewhere [9]. By approximating the friction drag by $-C_f Q/A$ and using the expression (3) for the pressure P, we can re-write the momentum equation (2) as

$$\frac{\partial Q}{\partial t} + \frac{\partial}{\partial x}\left(\frac{Q^2}{A} + \frac{\beta}{3\rho}A^{\frac{3}{2}}\right) = -C_f\frac{Q}{A} + C_v\frac{\partial^2 Q}{\partial^2 x}. \tag{4}$$

We set $C_f = 22\pi\nu$ as was computed from coronary blood flow in [10] and we define $C_v = \frac{A\nu_s}{\rho}$.

From a mathematical point of view, the system of equations (1)-(4) can be decomposed in a hyperbolic subproblem (transport equation) and a parabolic subproblem (viscoelastic source term). To obtain the numerical solution of both subproblems, we introduce a mesh in the axial direction by dividing each artery in a series of cells of size Δx. We then define the discrete time $t^n = n\Delta t$, where Δt is the time step. Using this decomposition of the space and time domains, we discretize the hyperbolic subproblem with a MUSCL (monotonic upwind scheme for conservation law) finite volume scheme and the parabolic subproblem with a Crank-Nicolson scheme. We compute the numerical solution using a code developed in our laboratory, written in C++ and parallelized with OpenMP. The numerical implementation of the full viscoelastic nonlinear system has been validated by comparing the computed solutions to analytic solutions of the linearized system and to experimental data [11, 9].

The network used in the numerical simulations is constructed by connecting different arterial segments together. These connections take place at branching points. As an example, we considered a simple branching problem: a single parent vessel connected to two daughter arteries. In this configuration, there are six unknowns at the iteration $n+1$ (numerically speaking, n refers to time t^n and $n+1$ to time t^{n+1}): A_p^{n+1} and Q_p^{n+1} for the outlet of the parent artery and $A_{d_1}^{n+1}$, $Q_{d_1}^{n+1}$, $A_{d_2}^{n+1}$ and $Q_{d_2}^{n+1}$ for the inlets of the two daughter arteries. These quantities are function of the values at the iteration n. To determine these unknowns, we impose the basic laws of conservation at the branching point, that is the conservation of mass flux

$$Q_p^{n+1} - Q_{d_1}^{n+1} - Q_{d_2}^{n+1} = 0,$$

and the continuity of total pressure

$$\frac{1}{2}\rho\left(\frac{Q_p^{n+1}}{A_p^{n+1}}\right)^2 + P_p^{n+1} - \frac{1}{2}\rho\left(\frac{Q_{d_i}^{n+1}}{A_{d_i}^{n+1}}\right)^2 - P_{d_i}^{n+1} = 0.$$

The pressures P are expressed as a function of the cross-sectional area A using the constitutive relation (3). By matching at the branching point the incoming and outgoing characteristics of the hyperbolic subproblem, we obtain the last three

equations we need to complete the resolution of the branching point problem. Energy losses should be taken into account due to the complex flow in the branching sites but, in practice, these losses have only secondary effects on the pulse waves [8], therefore we neglect them.

To drive the flow through the network, we prescribe inlet and outlet boundary conditions. These boundary conditions are: (i) an imposed physiological flow rate at the inlet of the ascending aorta and (ii) reflection coefficients imposed at the outlet of each terminal segment and characterizing the resistance of the vascular bed that is not taken into account in our model. Theses values are given in the last column of Table A.1 in Appendix A. The input flow rate signal we use in the numerical simulations is

$$Q(t) = \begin{cases} Q_{max} \sin(\frac{2\pi}{T} t) & \text{if } t \leq T/2; \\ 0. & \text{if } t > T/2. \end{cases}$$

where T is the period of the heart cycle. To define the maximum flow rate Q_{max}, we introduce the ejection fraction EF, defined as

$$EF = \frac{EDV - ESV}{EDV} \times 100, \tag{5}$$

where EDV is the End Diastolic Volume and ESV is the End Systolic Volume. Healthy people typically have an EF between 50% and 65%. On the contrary, people with heart muscles damages (principally on the myocardium) have a low EF. The ejected volume $V_e = EDV - ESV$ during one period is computed by integrating $Q(t)$ over one period

$$V_e = Q_{max} \frac{T}{\pi}. \tag{6}$$

Finally we have

$$Q_{max} = EF\ \pi\ \frac{EDV}{T}, \tag{7}$$

and we can now define Q_{max}, for a given period T and a given EDV as a function of EF. With this approach we propose a simple heart model that allows us to define a pathological heart by reducing EF. This behavior is physiologically meaningful if in the case of a pathological heart, the system reacts by either increasing EDV by expanding the muscle fibers or by reducing the period T by increasing the cardiac rhythm.

3. Numerical methods and results

In this section we present the numerical protocol and detail the numerical results obtained with the healthy network, the pathological network presenting an obstruction of the Right Iliac artery and the pathological network treated with three different bypass grafts (Axillo-Femoral, Femoral-Femoral and cross-over Femoral bypass grafts).

The numerical protocol is the following:

1. we first simulate blood flow in a healthy network (Figure 1 (a)). We use the computed numerical data as the target blood flow we compare the other numerical results to;
2. we then build the pathological network by narrowing the cross-sectional area of the Right Iliac artery (Figure 1 (b)). As we record all hemodynamic variables everywhere in the network for different degrees of obstruction of the stenosis, we are able to observe the global changes depending on the degree of obstruction;
3. we finally build three repaired networks by introducing in the pathological network the Axillo-Femoral, Femoral-Femoral and cross-over Femoral bypass grafts using elastic tubes inserted between the donor and the receptor arteries of each bypass graft (Figure 1 (c) for the Axillo-Femoral, the other two are presented in Figure 3). We then compare the numerical results obtained with the three repaired networks to those obtained with pathological and healthy networks.

The key points of clinical repair are first the ability of the bypass graft to restore blood flow in the previously non-perfused region (here the network downstream of Right Femoral artery, number 52 in Figure 1), and second, ensuring that the repair does not ill-balance the rest of the hemodynamic circulation. In the following, both key points are systematically for each repaired network.

3.1. Healthy state

The healthy network we consider represents the principal arteries of the great circulation (55 segments). It is used in the literature as the basic model of the systemic network. Its topology is presented in Figure 1 (a), where every artery is given a number (ID) useful to understand the numerical results. Each artery of the healthy network is described by geometrical and mechanical parameters adapted from [12] and presented in Table A.1. Compared to [12], we have added a viscoelastic term to the wall model. This viscoelastic term exists in physiological conditions and is very important from the hemodynamic point of view [8, 9]. Without it, high frequency components would be present in the pulse wave signal [9]. In the literature on 1D network models, this viscoelastic term is usually not included as its coefficients are hard to evaluate experimentally. Here, we use the work of [13], where the viscosity of the aortic walls

of dogs was modeled by a Kelvin-Voigt model and where the values of ϕ range between $3.8 \pm 1.3 \times 10^3$ Pa $\cdot$ s and $7.8 \pm 1.1 \times 10^3$ Pa $\cdot$ s. Hence, in all numerical simulations we assume $\phi = 5 \times 10^3$ Pa $\cdot$ s to calculate the coefficient C_v.

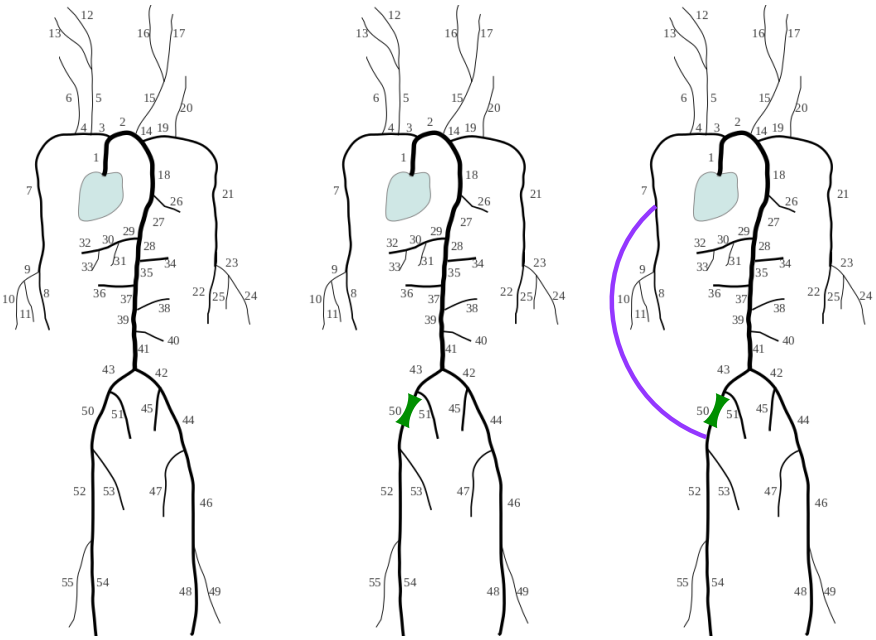

Figure 1. Arterial tree. (a) "Healthy" network. (b) Pathological network. (c) "Repaired" network. The pathological network (b) is modeled by narrowing the cross-sectional area of the Right Iliac artery (number 50, green) and the extracorporeal bypass graft by an elastic tube (purple). In each segment, a 1D model of fluid flow with viscoelastic wall is solved numerically. The flow is imposed by given heart pulses, with a realistic reflection coefficient at the end of each terminal arteries. Table A.1 presents the geometrical and mechanical data used in numerical computations.

The flow in each arterial segment is computed using the 1D numerical model presented in the previous section. The simulations are performed over 10 heart periods. Any data we present is taken from the final period to ensure that a permanent state is reached, where each heart period is identical to the next. The recorded data for the healthy network contains the values of the blood flow rate $Q_{healthy}$, the cross-sectional area $A_{healthy}$ and the blood pressure $P_{healthy}$ in every artery and at every recorded time of the final period. These numerical results are the target values we use from now on to evaluate the severity of the pathological situation and to assess the restorative properties of the bypass grafts.

3.2. Pathological case

3.2.1. Numerical protocol

We model the stenosis by narrowing the cross-sectional area of a portion of the Right Iliac artery (number 50 in Figure 1 (b)). The length of the occlusion is 5 *cm* and the degree of obstruction is directly related to the ratio of the cross-sectional area of the stenosed artery $A_{\%}$ over the cross-sectional area of the healthy artery $A_{healthy}$. We define this ratio as $I_s = \frac{A_{healthy} - A_{\%}}{A_{healthy}} \times 100$. Four control sites are chosen to evaluate the hemodynamical influence of the stenosis on the flow rate and pressure waveforms. Two are located in the lower legs, in the Right Femoral artery (number 52) and

in Left Femoral artery (number 46). The other two are located in the arms, in the Right Subclavian artery (number 7) and in the Left Subclavian artery (number 21). The Right Femoral artery (number 52) is the principal assessment point of our numerical study as the flow rate passing through it characterizes the leg's perfusion and therefore the degree of ischemia. The other control sites (Left Femoral, Left and Right Subclavian) are used in clinical routines to evaluate if a bypass graft surgery is successful.

3.2.2. Results

Figure 2 (a) shows the variation with the degree of obstruction I_s of the blood flow rate Q averaged over the final period at the four previously defined control sites. The first observation is that under 60% to 70% of obstruction there is no significant variation of flow rate with respect to the healthy state (I_s = 0%). This behavior is well known in the medical community (i.e. renal arteries in pigs and human carotid arteries [14, 15]). Above 70% of obstruction, the flow rate drastically decreases in the Right Femoral artery (number 52) due to the obstruction of its proximal artery, the Right Iliac artery (number 50). We note that for an occlusion of 90% there is almost no blood flow in the Right Femoral artery (number 52). Conversely, the flow rate moderately increases in the other control sites to compensate for the reduction of flow rate in the network distal to the stenosis. This as a clear example of how we can monitor global variations in the network caused by a local perturbation.

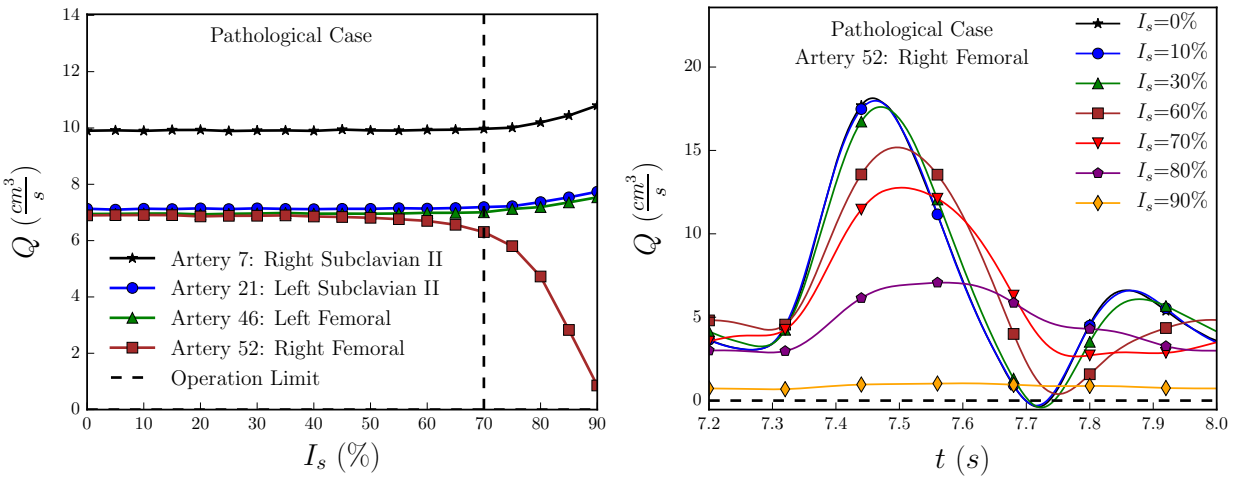

Figure 2. (a) Flow rate averaged over a cycle as function of the obstruction degree I_s for the following arteries: Right Femoral, (number 52), Left Femoral, (number 46), Right Subclavian (number 7) and Left Subclavian, (number 21). As the ratio I_s increases, the flow rate drops in the Right Femoral artery, distal to the stenosis, whereas the flow rate increases in all other segments to compensate this drop. (b) Instantaneous flow rate as function of time over a cycle in the Right Femoral artery (number 52) for different degree of obstruction. As the ratio I_s increases, the waveform looses its pulsatility and flattens and the average flow rate drops.

Figure 2 (b) presents the time evolution of the blood flow rate Q over the final period in the Right Femoral artery (artery 52). These results are correlated to those of Figure 2 (a) but provide additional information: first, as expected,

the flow rate decreases in average as the ratio I_s increases; second the positions of the maximum and minimum peaks are shifted, due to a time shift in the traveling waves; third the maximum amplitude decreases significantly as the ration I_s increases and we observe that for $I_s = 70\%$ the amplitude drops by 30% and for $I_s = 80\%$ it drops by 60%. For $I_s = 90\%$, the amount of blood perfusion in the leg is minimal and the waveform is a flat line. This last point indicates that as the degree of obstruction I_s increases, the signal looses its pulsatility and flattens.

3.3. Bypass grafts

3.3.1. Numerical protocol

We study here the three most commonly used bypass grafts to treat a stenosis of the Right Iliac arteries: the Axilo-Femoral (AxF) where the donor artery is the Axillary artery (artery 7), the cross-over Femoral (FF) where the donor artery is the opposite Common Femoral artery (artery 44) and the Aorto-Femoral (ArF) where the donor artery is the Abdominal Aorta (artery 39). Each bypass graft is connected to the pathological network using two connection points: the proximal anastomosis, connecting the bypass graft to the donor artery, and the distal anastomosis, linking the bypass graft to the receptor artery. For each of these three bypass grafts, the distal anastomosis is located downstream of the stenosis, in the distal part of the Right Iliac artery (artery 50). In Figure 3 we represent the topology of the three different pathological network treated with a bypass graft.

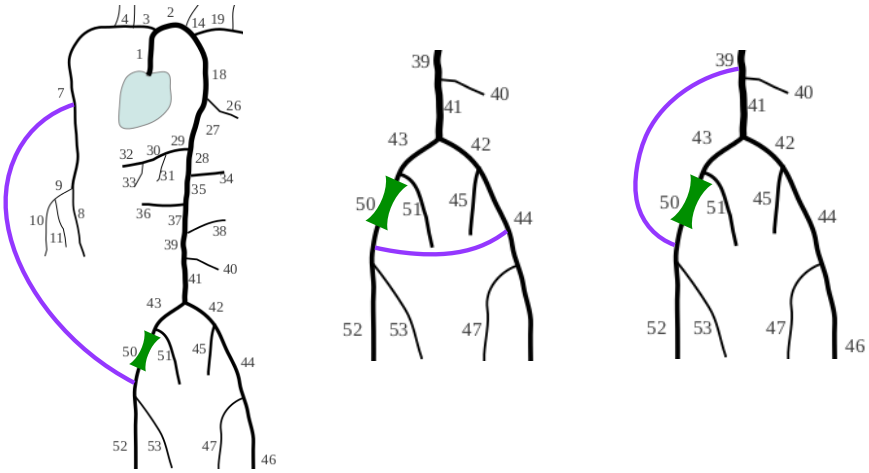

Figure 3. Sketch of three bypasses with the donor artery : (left) Axillo-Femoral (AxF) and donor artery, Right Axillary artery (number 7), (center) cross-over-Femoral (FF) and donor artery, Left Femoral artery (number 44) and (right) Aorto-Femoral (ArF) and donor artery, Abdominal Aorta (numer 39).

Each bypass graft we study is made of the same composite material which is constituted principally of polyethylene terephthalate (Dacron). From the literature [16], we obtain their mechanical and geometrical characteristics, that is a Young's modulus equal to 9×10^6 *Pa*, an internal diameter of 0.8 *cm* and a thickness of 0.05 *cm*. The length L of each

bypass graft depends on the geometric distance between the proximal and distal anastomoses: Axillo-Femoral, 40 *cm*, cross-over-Femoral, 20 *cm* and Aorto-Femoral, 20 *cm*.

To assess the performances of each bypass graft, we define three control sites where we compare the healthy, pathological and repaired data. The first is located in the Right Femoral artery (number 52), downstream of the stenosis and the distal anastomosis, and is identical to the control site used previously to analyze the pathological network. The second and third control sites are respectively situated in the upstream and downstream segments of the proximal anastomosis.

3.3.2. Results

For each bypass graft we first study the predicted perfusion hemodynamics in the first control site located downstream of the stenosis, in the Right Femoral artery (number 52). Figure 4 (a) presents the evolution with the degree of obstruction I_s of the time-averaged blood flow rate in the pathological network (same as Figure 2 (a) for the artery 52) and in the three repaired networks obtained using the AxF, ArF and FF bypass grafts. Figure 4 (b) shows the temporal evolution of the blood flow rate over the final heart cycle for I_s = 90 %. These figures should be compared to Figures 2 (a) and 2 (b). We observe in Figure 4 (a) that for all three bypass grafts configurations, we retrieve in average the blood flow rate of the healthy case for every value of I_s considered. Figure 4 (b) indicates that the repaired waveforms are similar to the target healthy one although the amplitudes of the peaks are a slightly underestimated. The delay in the position of the maximum and minimum flow rate peaks is caused by a change in the length of vessel traveled by the wave starting from the heart. Overall we retrieve for all three bypass graft configurations the target average blood flow rate as well as the approximate shape of the waveform. From the analysis of Figure 4 we conclude that all three bypass graft are successful in retrieving the healthy flow rate in the first control site distal to the obstructed segment (Right Femoral artery 52).

We complete our study by analyzing the time-averaged blood flow rate in each donor artery. In the subsequent numerical results we focus on the remaining two control sites: the upstream and downstream segments of the proximal anastomosis, which differ from one bypass graft configuration to the next. We expect that each bypass graft will supply the missing blood flow rate to the diseased lower leg (Right Femoral artery 52) whilst maintaining a healthy perfusion in the donor site (downstream segments of the proximal anastomosis).

For the FF bypass graft the donor artery is the opposite Femoral artery (Left Femoral artery, number 44 in Figure 1). Figure 5 presents the evolution of the time-averaged blood flow rate with the degree of obstruction I_s in the two control sites, upstream and downstream of the proximal anastomosis. We observe that upstream of the donor site the flow rate increases proportionally to the degree of obstruction. Indeed the donor artery must know supply blood to both its downstream segment and the stenosed member and therefore increases its flow rate, in comparison with the

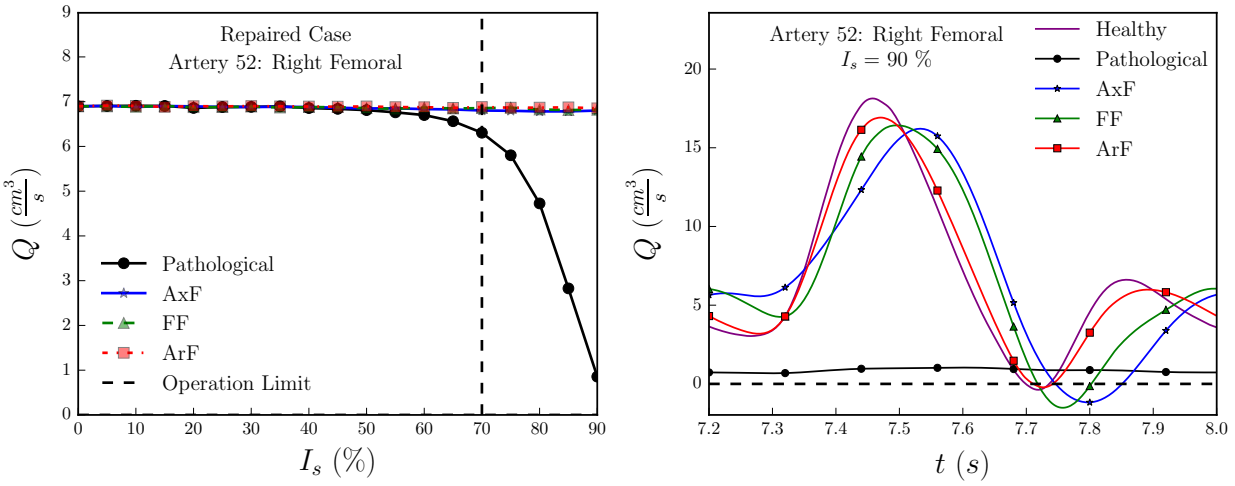

Figure 4. (a) Averaged flow rate over a cycle as function of the degree of obstruction I_s (Artery 52 : Right Femoral) (b) Instantaneous flow rate as function of time over a cycle (Artery 52 : Right Femoral) for healthy, pathological with $I_s = 90\%$ and for the three bypasses. We observe that for all three bypass graft configurations, we are able to recover the target healthy flow rate (average values and waveform) distal to the stenosis.

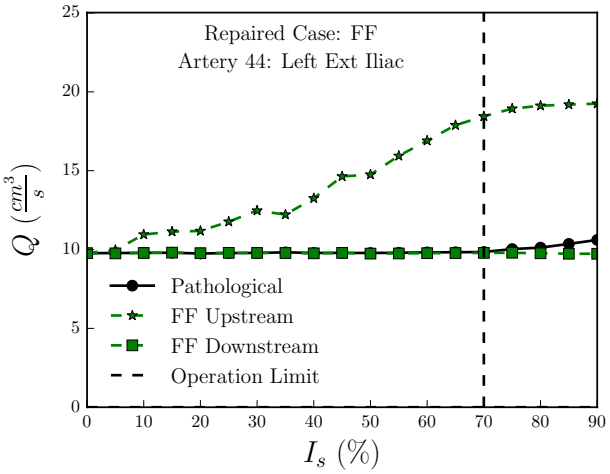

Figure 5. Cross-over Femoral bypass graft: average flow rate over a cycle in the opposite Femoral artery (Artery 44). Upstream of the proximal anastomosis, the flow rate increases to properly vascularize the bypass graft, depending on the degree of obstruction I_s. Downstream of the proximal anastomosis, we recover the healthy ($I_s = 0\%$) flow rate.

healthy case ($I_s = 0\%$). The downstream blood flow rate does not change compared to the healthy case ($I_s = 0\%$) indicating that the opposite lower leg, downstream of the proximal anastomosis, is correctly supplied. We note that for a severe stenosis (obstruction of 90 %) the upstream blood flow rate is twice the basal one.

For the ArF bypass graft the donor artery is the Abdominal Aorta (artery 39), the principal path carrying blood to both lower legs. Figure 6 presents the evolution of the time-averaged blood flow rate with the degree of obstruction I_s in the two control sites, upstream and downstream of the proximal anastomosis. We observe that upstream of the proximal anastomosis, the blood flow rate does not change with the degree of obstruction I_s, contrary to the FF bypass

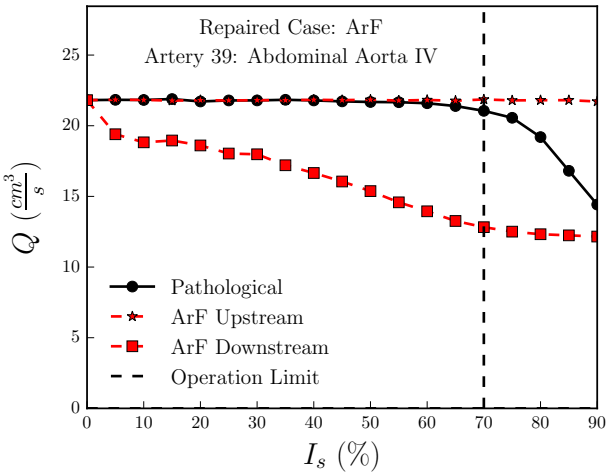

Figure 6. Aorto-Femoral bypass graft: average flow rate over a cycle at the donor artery (Artery 39). Upstream of the proximal anastomosis, the flow rate remains unchanged since blood flow passing through the bypass graft to vascularize the right leg was already supplied by the Aorta in the healthy case. Downstream of the proximal anastomosis, the flow rate decreases with the degree of obstruction I_s since now only the blood supplying the left leg is passing downstream of the proximal anastomosis.

graft configuration. Indeed, in the healthy configuration the Abdominal Aorta already carries blood the the Right Femoral artery, therefore no compensation mechanism is required upstream of the donor site. Conversely we observe that the downstream of the proximal anastomosis, the blood flow rate decreases as the degree of obstruction increases, in comparison to the healthy configuration ($I_s = 0\%$). Indeed, since the blood that supplies the stenosed member (Right Femoral artery 52) now flows through the bypass graft, only the blood supply for the left leg remains downstream of the donor site. This behavior shows that the bypass graft is indeed carrying blood the stenosed member. Finally, we note that in absence of stenosis ($I_s = 0\%$) the downstream blood flow is symmetrically shared between the two legs and that for a severe stenosis ($I_s = 90\%$) the downstream blood flow rate is half the basal one.

Figure 7 presents the evolution for the AxF bypass graft of the time-averaged blood flow rate with the degree of obstruction I_s in the two control sites, upstream and downstream of the proximal anastomosis. The results are identical to those obtained with the FF bypass graft (Figure 5). The same analysis can be performed and we conclude that this bypass graft configuration correctly supplies the stenosed member while maintaining the healthy flow rate downstream of the donor site. We also note that for an obstruction of 90% the upstream blood flow rate is twice the basal one.

These results show that for all three bypass graft configurations, the target behaviors are obtained and the bypass graft surgery is successful.

3.4. Optimization

Of the three bypass grafts considered here, the AxF has the highest chance of graft failure. Indeed, the AxF is the longest bypass graft. Moreover, the AxF bypass graft surgery is performed on patients who are not healthy enough to

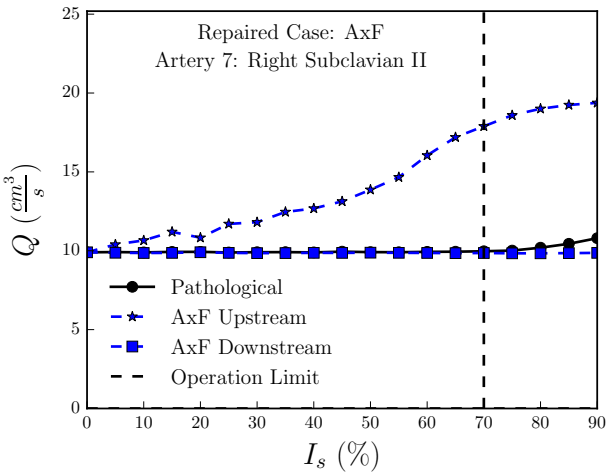

Figure 7. Axillo-Femoral bypass graft: averaged flow rate over a cycle at the donor artery (number 7). Upstream of the proximal anastomosis, the flow rate increases to properly vascularize the bypass graft, depending on the degree of obstruction I_s. Downstream of the proximal anastomosis, we recover the healthy ($I_s = 0\%$) flow rate.

survive the more invasive surgical procedures required to implement the FF or ArF bypass grafts.

For these reasons we choose to perform a detailed analysis to determine the optimal mechanical (the Young modulus E) and geometrical (the radius R) parameters of the AxF bypass graft. In order to give arguments for discussion we perform hundreds of simulations where we vary the values of the Young modulus $[0.1 - 50\ MPa]$ and radius R $[0.01 - 5\ cm]$ of the AxF bypass graft. As before, we use as a target the healthy data in the Right Femoral artery (number 52 in Figure 1).

Figures 8 presents a log-log scale contour plot of the normalized flow rate $\frac{Q}{Q_{healthy}}$ in the AxF bypass graft obtained for different values of the Young modulus E and the radius R in a pathological network with $I_s = 90\ \%$. The red circle in the middle of the Figure 8 indicates the actual values of the bypass graft's Young's modulus E and radius R. For these values the normalized flow rate $\frac{Q}{Q_{healthy}} \approx 100\%$ indicating that the healthy flow rate is restored in average downstream of the stenosis. Starting from this point we analyze the results by moving along the horizontal and vertical directions, that is for E constant and varying R (horizontal) and for R constant and varying E (vertical).

For a constant Young's modulus E, we analyze the effect of changing the radius R of the bypass graft. Moving along the horizontal direction towards the left starting from the red circle, the radius R decreases. Consequently the hydraulic resistance of the bypass graft increases leading to a decrease of the the normalized flow rate $\frac{Q}{Q_{healthy}}$. Moving now towards the right, the radius R increases. Even though for a large range of values of the Young's modulus E the value of $\frac{Q}{Q_{healthy}}$ is close to 100%, it is clear that as the radius increase the blood volume inside of the bypass also increases. This results in a decrease of the flow rate distal to the proximal anastomosis and could lead to the ischemia of the right hand. Increasing the radius R also implies decreasing blood flow velocity in the bypass graft which results

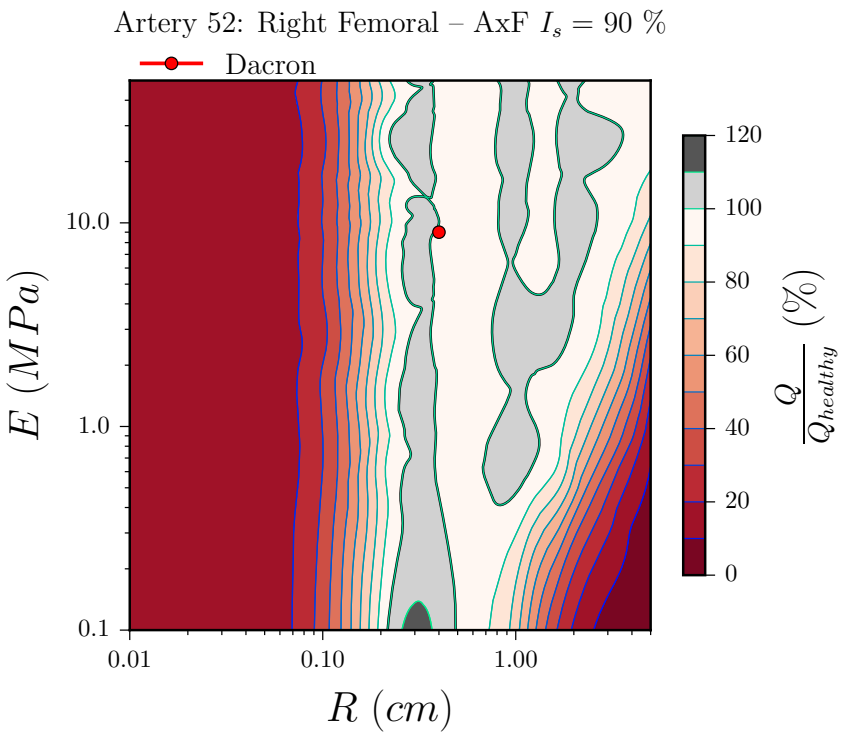

Figure 8. Contour plot for the normalized time-averaged flow rate $\frac{Q}{Q_{healthy}}$ as function of the Young modulus E and the radius R for a stenosis of I_s = 90 %. The red circle corresponds to the actual values of the Young modulus E and the radius R used in numerical simulations, which are situated in an optimal zone (100%). When the radius decreases, the resistance of the tube increases and therefore less flow is bypassing through the bypass graft. When the Young's modulus decreases, the tube becomes more compliant and stores more flow. Both behaviors reduce the quality of the bypass graft.

in a smaller shear rate along the bypass. This increases aggregation and coagulation processes which are key factors in the onset of graft failure. From a physiological and mechanical point of view for a given value of the Young's modulus E, the optimal radius R should be taken from a $\frac{Q}{Q_{healthy}} \approx 100\%$ region and be as small as possible to ensure an optimal distal and proximal blood perfusion.

For a constant radius R, we analyze the effect of changing the Young's modulus E of the bypass graft. Moving along the vertical direction towards the top or the bottom starting from the red circle, $\frac{Q}{Q_{healthy}} \approx 100\%$ for every value of the Young's modulus E. However, the bypass graft's Young's modulus E should be taken as close as possible to the arteries' Young's modulus since elasticity jumps lead to impedance discontinuities and therefore higher reflected pressure waves. Moreover, if the bypass graft's elasticity is too small, the bypass graft will become more compliant and inflate, increasing the blood volume inside the bypass graft. Conversely, if the bypass graft's elasticity is too large, high pressure peaks will be generated due to increased wave reflections.

Figures 9 presents a log-log scale contour plot of the normalized peak to peak flow rate $\frac{Q_{max}-Q_{min}}{Q_{max}^{healthy}-Q_{min}^{healthy}} \frac{Q_{healthy}}{Q}$ in the AxF bypass graft obtained for different values of the Young modulus E and the radius R in a pathological network

with an obstruction degree of 90 %. This quantity measures the pulsatility of the flow rate signal (and consequently the pressure signal). We observe that both Figure 8 and Figure 9 are similar, and the previous analysis of Figure 8 can be applied. Nevertheless, Figure 9 provides additional information especially in the region of large radii. For a fixed Young's modulus E, increasing the radius significantly decreases the value of $\frac{Q_{max}-Q_{min}}{Q^{healthy}_{max}-Q^{healthy}_{min}}\frac{Q_{healthy}}{Q}$. We previously described this situation as a correlation between an increase of radius and an increase of the blood volume inside the bypass graft. We prove here that this increase in blood volume in the bypass graft reduces its quality as the signal looses its pulsatility.

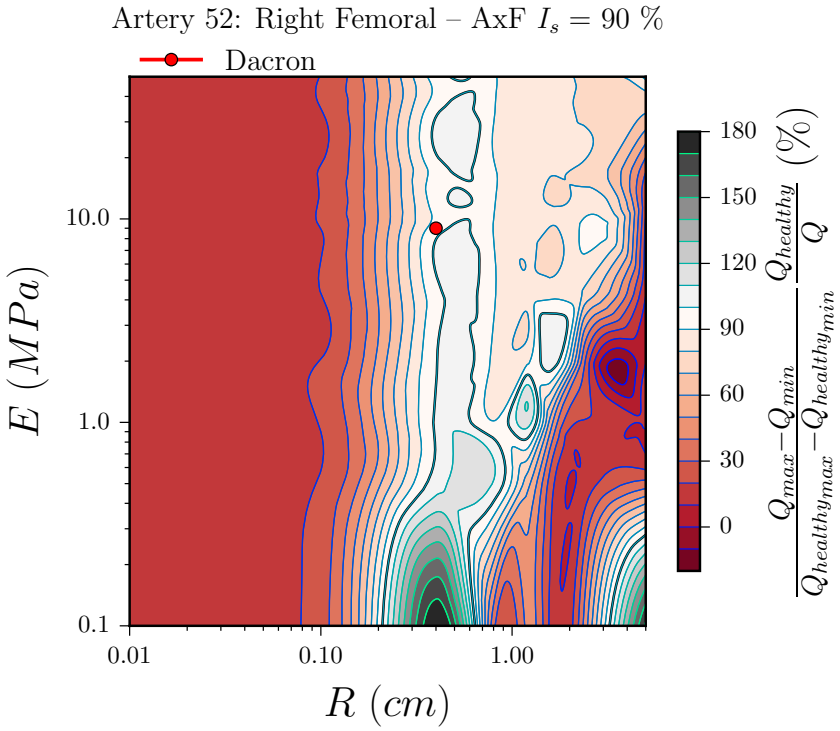

Figure 9. Contour plot for the normalized peak to peak flow rate $\frac{Q_{max}-Q_{min}}{Q^{healthy}_{max}-Q^{healthy}_{min}}\frac{Q_{healthy}}{Q}$ as function of the Young modulus E and the radius R for a stenosis of 90 %. The red circle corresponds to the actual values of the Young modulus E and the radius R used in numerical simulations.

4. Conclusion

We presented a model network comprising 55 viscoelastic arteries in which we modeled blood flow using a 1D fluid-structure system of equations. We performed simulations of this complex nonlinear dissipative system in a healthy and a pathological network presenting a stenosis of the Right Iliac artery. We then computed blood flow in a repaired network where we considered the three classical bypass grafts used to treat a stenosis of the Iliac artery. Our numerical results showed that all three bypass grafts are able to retrieved the healthy hemodynamics downstream of

the stenosed member whilst maintaining a global healthy circulation.

However, little is known about the evolution of the hemodynamics in a bypass graft when its geometrical and mechanical characteristics are changed. We therefore studied the optimization of the geometrical and mechanical characteristics of the Axillo-Femoral bypass. Indeed, this bypass graft is used on unhealthy weak patients who can not sustain other types of bypass graft surgeries and because it has the smallest graft survival time of the three studied bypass grafts. The optimization results (Figures 8 and 9) indicated that the mechanical characteristic of the bypass grafts used by clinicians are optimal and allow to retrieve the healthy circulation in the pathological network. Moreover, the numerical findings showed that choosing another set of parameters would lead to diminished performances of the bypass graft.

Besides the numerical approach, our numerical findings over an "averaged patient" proved that numerical hemodynamic predictions could be used to optimize or plan surgeries for specific patients, under the conditions that the pathologies were well defined and the physiological parameters known. Indeed, the numerical tool is very fast in terms of computing time, and therefore is suited for computational intensive simulations such as parametric analyses and error propagation tasks, and for the evaluation of new bypass procedures.

References

[1] L. Norgren, W. R. Hiatt, J. A. Dormandy, M. R. Nehler, K. A. Harris, F. G. R. Fowkes, Inter-society consensus for the management of peripheral arterial disease (TASC II), European Journal of Vascular and Endovascular Surgery 33 (1) (2007) S1–S75. doi:10.1016/j.ejvs.2006.09.024. URL http://www.sciencedirect.com/science/article/pii/S1078588406005351

[2] W. M. Abbott, A. Callow, W. Moore, R. Rutherford, F. Veith, S. Weinberg, Evaluation and performance standards for arterial prostheses, Journal of vascular surgery 17 (4) (1993) 746–756.

[3] E. Marchandise, M. Willemet, V. Lacroix, A numerical hemodynamic tool for predictive vascular surgery, Medical Engineering and Physics 31 (1) (2009) 131–144.

[4] M. Willemet, V. Lacroix, E. Marchandise, Validation of a 1d patient-specific model of the arterial hemodynamics in bypassed lower-limbs: Simulations against in vivo measurements, Medical Engineering & Physics 35 (11) (2013) 1573–1583. doi:10.1016/j.medengphy.2013.04.012. URL http://www.sciencedirect.com/science/article/pii/S1350453313001057

[5] N. Appleton, D. Bosanquet, G. Morris-Stiff, H. Ahmed, P. Sanjay, M. Lewis, Extra-anatomical bypass grafting – a single surgeon's experience, Annals of The Royal College of Surgeons of England 92 (6) (2010) 499–502. doi:10.1308/003588410X12664192076890. URL http://www.ncbi.nlm.nih.gov/pmc/articles/PMC3182793/

[6] S. E. Greenwald, C. L. Berry, Improving vascular grafts: the importance of mechanical and haemodynamic properties, The Journal of Pathology 190 (3) (2000) 292–299. doi:10.1002/(SICI)1096-9896(200002)190:3<292::AID-PATH528>3.0.CO;2-S. URL http://onlinelibrary.wiley.com/doi/10.1002/(SICI)1096-9896(200002)190:3<292::AID-PATH528>3.0.CO;2-S/abstract

[7] S. E. Musicant, M. E. Giswold, C. J. Olson, G. J. Landry, L. M. Taylor, R. A. Yeager, J. M. Edwards, G. L. Moneta, Postoperative duplex scan surveillance of axillofemoral bypass grafts, Journal of Vascular Surgery 37 (1) (2003) 54–61. doi:10.1067/mva.2003.43. URL http://linkinghub.elsevier.com/retrieve/pii/S0741521402751847

[8] J. Alastruey, A. Khir, K. Matthys, P. Segers, S. Sherwin, P. Verdonck, K. Parker, J. Peiró, Pulse wave propagation in a model human arterial network: Assessment of 1-d visco-elastic simulations against *in vitro* measurements, Journal of Biomechanics.

[9] X.-F. Wang, S. Nishi, M. Matsukawa, A. Ghigo, P.-Y. Lagrée, J.-M. Fullana, Fluid friction and wall viscosity of the 1d blood flow model, Journal of Biomechanics (2016) –doi:http://dx.doi.org/10.1016/j.jbiomech.2016.01.010.
URL http://www.sciencedirect.com/science/article/pii/S0021929016000191

[10] N. Smith, A. Pullan, P. Hunter, An anatomically based model of transient coronary blood flow in the heart, SIAM Journal on Applied mathematics 62 (3) (2002) 990–1018.

[11] M. Saito, Y. Ikenaga, M. Matsukawa, Y. Watanabe, T. Asada, P.-Y. Lagrée, One-dimensional model for propagation of a pressure wave in a model of the human arterial network: Comparison of theoretical and experimental results, Journal of Biomechanical Engineering 133 (2011) 121005.

[12] S. Sherwin, L. Formaggia, J. Peiro, V. Franke, Computational modelling of 1d blood flow with variable mechanical properties and its application to the simulation of wave propagation in the human arterial system, International Journal for Numerical Methods in Fluids 43 (6-7) (2003) 673–700.

[13] R. Armentano, J. Barra, J. Levenson, A. Simon, R. Pichel, Arterial wall mechanics in conscious dogs: assessment of viscous, inertial, and elastic moduli to characterize aortic wall behavior, Circulation Research 76 (3) (1995) 468–478.

[14] G. Lanzino, A. A. Rabinstein, R. D. Brown, Treatment of carotid artery stenosis: Medical therapy, surgery, or stenting?, Mayo Clinic Proceedings 84 (4) (2009) 362–368.
URL http://www.ncbi.nlm.nih.gov/pmc/articles/PMC2665982/

[15] N. Rognant, O. Rouvière, M. Janier, Q. H. Lê, P. Barthez, M. Laville, L. Juillard, Hemodynamic responses to acute and gradual renal artery stenosis in pigs, American Journal of Hypertension 23 (11) (2010) 1216–1219. doi:10.1038/ajh.2010.147.
URL http://ajh.oxfordjournals.org/content/23/11/1216

[16] S. Sarkar, H. J. Salacinski, G. Hamilton, A. M. Seifalian, The mechanical properties of infrainguinal vascular bypass grafts: Their role in influencing patency, European Journal of Vascular and Endovascular Surgery 31 (6) (2006) 627–636. doi:10.1016/j.ejvs.2006.01.006.
URL http://www.ejves.com/article/S1078588406000529/abstract

Appendix A. Wall Model and Geometrical and mechanical parameters of the network

The Table A.1 presents the name (ID), name, length, neutral cross-sectional area A_0 and mechanical parameters used in the network.

Table A.1: Arterial network: Data adapted from [12] and [13]

ID	Name	l (cm)	A_0 (cm^2)	β (10^6Pa/cm)	C_v ($10^4 cm^2$/s)	R_t
1	Ascending aorta	4.0	6.789	0.023	0.352	–
2	Aortic arch I	2.0	5.011	0.024	0.317	–
3	Brachiocephalic	3.4	1.535	0.049	0.363	–
4	R.subclavian I	3.4	0.919	0.069	0.393	–

Table A.1: Arterial network: Data adapted from [12] and [13]

ID	Name	l (cm)	A_0 (cm^2)	β (10^6Pa/cm)	C_v ($10^4 cm^2/s$)	R_t
5	R.carotid	17.7	0.703	0.085	0.423	–
6	R.vertebral	14.8	0.181	0.470	0.595	0.906
7	R. subclavian II	42.2	0.833	0.076	0.413	–
8	R.radius	23.5	0.423	0.192	0.372	0.82
9	R.ulnar I	6.7	0.648	0.134	0.322	–
10	R.interosseous	7.9	0.118	0.895	0.458	0.956
11	R.ulnar II	17.1	0.589	0.148	0.337	0.893
12	R.int.carotid	17.6	0.458	0.186	0.374	0.784
13	R. ext. carotid	17.7	0.458	0.173	0.349	0.79
14	Aortic arch II	3.9	4.486	0.024	0.306	–
15	L. carotid	20.8	0.536	0.111	0.484	–
16	L. int. carotid	17.6	0.350	0.243	0.428	0.784
17	L. ext. carotid	17.7	0.350	0.227	0.399	0.791
18	Thoracic aorta I	5.2	3.941	0.026	0.312	–
19	L. subclavian I	3.4	0.706	0.088	0.442	–
20	L. vertebral	14.8	0.129	0.657	0.704	0.906
21	L. subclavian II	42.2	0.650	0.097	0.467	–
22	L. radius	23.5	0.330	0.247	0.421	0.821
23	L. ulnar I	6.7	0.505	0.172	0.364	–
24	L. interosseous	7.9	0.093	1.139	0.517	0.956
25	L. ulnar II	17.1	0.461	0.189	0.381	0.893
26	intercoastals	8.0	0.316	0.147	0.491	0.627
27	Thoracic aorta II	10.4	3.604	0.026	0.296	–
28	Abdominal aorta I	5.3	2.659	0.032	0.311	–
29	Celiac I	2.0	1.086	0.056	0.346	–
30	Celiac II	1.0	0.126	0.481	1.016	–
31	Hepatic	6.6	0.659	0.070	0.340	0.925

Table A.1: Arterial network: Data adapted from [12] and [13]

ID	Name	l (cm)	A_0 (cm^2)	β (10^6Pa/cm)	C_v ($10^4 cm^2/s$)	R_t
32	Gastric	7.1	0.442	0.096	0.381	0.921
33	Splenic	6.3	0.468	0.109	0.444	0.93
34	Sup. mensenteric	5.9	0.782	0.083	0.439	0.934
35	Abdominal aorta II	1.0	2.233	0.034	0.301	–
36	L. renal	3.2	0.385	0.130	0.481	0.861
37	Abdominal aorta III	1.0	1.981	0.038	0.320	–
38	R. renal	3.2	0.385	0.130	0.481	0.861
39	Abdominal aorta IV	10.6	1.389	0.051	0.358	–
40	Inf. mesenteric	5.0	0.118	0.344	0.704	0.918
41	Abdominal aorta V	1.0	1.251	0.049	0.327	–
42	R. com. iliac	5.9	0.694	0.082	0.405	–
43	L. com. iliac	5.8	0.694	0.082	0.405	–
44	L. ext. iliac	14.4	0.730	0.137	0.349	–
45	L. int. iliac	5.0	0.285	0.531	0.422	0.925
46	L. femoral	44.3	0.409	0.231	0.440	–
47	L. deep femoral	12.6	0.398	0.223	0.419	0.885
48	L. post. tibial	32.1	0.444	0.383	0.380	0.724
49	L. ant. tibial	34.3	0.123	1.197	0.625	0.716
50	L. ext. iliac	14.5	0.730	0.137	0.349	–
51	R. int. iliac	5.0	0.285	0.531	0.422	0.925
52	R. femoral	44.4	0.409	0.231	0.440	–
53	R. deep femoral	12.7	0.398	0.223	0.419	0.888
54	R. post. tibial	32.2	0.442	0.385	0.381	0.724
55	R. ant. tibial	34.4	0.122	1.210	0.628	0.716